Hovatta, Talvikki; Lähteenmäki, Anne; Tornikoski, Merja; VERITAS Collaboration

VERITAS Discovery of Very High Energy Gamma-Ray Emission from S3 1227+25 and Multiwavelength Observations

# VERITAS Discovery of Very High Energy Gamma-Ray Emission from S3 1227+25 and Multiwavelength Observations

A. Acharyya[1], C. B. Adams[2], A. Archer[3], P. Bangale[4], W. Benbow[5], A. Brill[6], J. L. Christiansen[7], A. J. Chromey[5], M. Errando[8], A. Falcone[9], Q. Feng[5], J. P. Finley[10], G. M. Foote[4], L. Fortson[11], A. Furniss[12], G. Gallagher[13], W. Hanlon[5], D. Hanna[14], O. Hervet[15], C. E. Hinrichs[5,16], J. Hoang[15], J. Holder[4], W. Jin[1], M. N. Johnson[15], P. Kaaret[17], M. Kertzman[3], D. Kieda[18], T. K. Kleiner[19], N. Korzoun[4], F. Krennrich[20], M. J. Lang[21], M. Lundy[14], G. Maier[19], C. E McGrath[22], M. J. Millard[17], J. Millis[13,23], C. L. Mooney[4], P. Moriarty[21], R. Mukherjee[24], S. O'Brien[14], R. A. Ong[25], M. Pohl[19,26], E. Pueschel[19], J. Quinn[22], K. Ragan[14], P. T. Reynolds[27], D. Ribeiro[11], E. Roache[5], I. Sadeh[19], A. C. Sadun[28], L. Saha[5], M. Santander[1], G. H. Sembroski[10], R. Shang[24], M. Splettstoesser[15], A. K. Talluri[11], J. V. Tucci[29], V. V. Vassiliev[25], D. A. Williams[15], S. L. Wong[14]

(The VERITAS Collaboration),

Talvikki Hovatta[30,31], Svetlana G. Jorstad[32], Sebastian Kiehlmann[33,34], Anne Lähteenmäki[31,35], Ioannis Liodakis[36], Alan P. Marscher[32], Walter Max-Moerbeck[37], Anthony C. S. Readhead[38], Rodrigo Reeves[39], Paul S. Smith[40], and Merja Tornikoski[31]

[1] Department of Physics and Astronomy, University of Alabama, Tuscaloosa, AL 35487, USA; aacharyya1@ua.edu, jmsantander@ua.edu
[2] Physics Department, Columbia University, New York, NY 10027, USA
[3] Department of Physics and Astronomy, DePauw University, Greencastle, IN 46135-0037, USA
[4] Department of Physics and Astronomy and the Bartol Research Institute, University of Delaware, Newark, DE 19716, USA
[5] Center for Astrophysics | Harvard & Smithsonian, Cambridge, MA 02138, USA
[6] NASA/Goddard Space-Flight Center, Code 661, Greenbelt, MD 20771, USA
[7] Physics Department, California Polytechnic State University, San Luis Obispo, CA 94307, USA
[8] Department of Physics, Washington University, St. Louis, MO 63130, USA
[9] Department of Astronomy and Astrophysics, 525 Davey Lab, Pennsylvania State University, University Park, PA 16802, USA
[10] Department of Physics and Astronomy, Purdue University, West Lafayette, IN 47907, USA
[11] School of Physics and Astronomy, University of Minnesota, Minneapolis, MN 55455, USA
[12] Department of Physics, California State University—East Bay, Hayward, CA 94542, USA
[13] Department of Physics and Astronomy, Ball State University, Muncie, IN 47306, USA
[14] Physics Department, McGill University, Montreal, QC H3A 2T8, Canada
[15] Santa Cruz Institute for Particle Physics and Department of Physics, University of California, Santa Cruz, CA 95064, USA
[16] Department of Physics and Astronomy, Dartmouth College, 6127 Wilder Laboratory, Hanover, NH 03755 USA
[17] Department of Physics and Astronomy, University of Iowa, Van Allen Hall, Iowa City, IA 52242, USA
[18] Department of Physics and Astronomy, University of Utah, Salt Lake City, UT 84112, USA
[19] DESY, Platanenallee 6, D-15738 Zeuthen, Germany
[20] Department of Physics and Astronomy, Iowa State University, Ames, IA 50011, USA
[21] School of Natural Sciences, University of Galway, University Road, Galway, H91 TK33, Ireland
[22] School of Physics, University College Dublin, Belfield, Dublin 4, Ireland
[23] Department of Physics, Anderson University, 1100 East 5th Street, Anderson, IN 46012, USA
[24] Department of Physics and Astronomy, Barnard College, Columbia University, New York, NY 10027, USA
[25] Department of Physics and Astronomy, University of California, Los Angeles, CA 90095, USA
[26] Institute of Physics and Astronomy, University of Potsdam, 14476 Potsdam-Golm, Germany
[27] Department of Physical Sciences, Munster Technological University, Bishopstown, Cork, T12 P928, Ireland
[28] Department of Physics, University of Colorado Denver, Campus Box 157, P.O. Box 173364, Denver, CO 80217, USA
[29] Department of Physics, Indiana University−Purdue University Indianapolis, Indianapolis, IN 46202, USA
[30] Finnish Centre for Astronomy with ESO (FINCA), University of Turku, FI-20014, Turku, Finland
[31] Aalto University Metsähovi Radio Observatory, Metsähovintie 114, 02540 Kylmälä, Finland
[32] Institute for Astrophysical Research, Boston University, 725 Commonwealth Avenue, Boston, MA 02215, USA
[33] Institute of Astrophysics, Foundation for Research and Technology-Hellas, GR-71110 Heraklion, Greece
[34] Department of Physics, Univ. of Crete, GR-70013 Heraklion, Greece
[35] Aalto University Department of Electronics and Nanoengineering, P.O. BOX 15500, FI-00076 AALTO, Finland
[36] Finnish Center for Astronomy with ESO, University of Turku, FI-20014, Finland
[37] Departamento de Astronomía, Universidad de Chile, Camino El Observatorio 1515, Las Condes, Santiago, Chile
[38] Owens Valley Radio Observatory, California Institute of Technology, Pasadena, CA 91125, USA
[39] Departamento de Astronomá, Universidad de Concepción, Concepción, Chile
[40] Steward Observatory, University of Arizona, 933 North Cherry Avenue, Tucson, AZ 85721-0065, USA

## Abstract

We report the detection of very high energy gamma-ray emission from the blazar S3 1227+25 (VER J1230+253) with the Very Energetic Radiation Imaging Telescope Array System (VERITAS). VERITAS observations of the source were triggered by the detection of a hard-spectrum GeV flare on 2015 May 15 with the Fermi-Large Area Telescope (LAT).

A combined 5 hr VERITAS exposure on May 16 and 18 resulted in a strong $13\sigma$ detection with a differential photon spectral index, $\Gamma = 3.8 \pm 0.4$, and a flux level at 9% of the Crab Nebula above 120 GeV. This also triggered target-of-opportunity observations with Swift, optical photometry, polarimetry, and radio measurements, also presented in this work, in addition to the VERITAS and Fermi-LAT data. A temporal analysis of the gamma-ray flux during this period finds evidence of a shortest variability timescale of $\tau_{obs} = 6.2 \pm 0.9$ hr, indicating emission from compact regions within the jet, and the combined gamma-ray spectrum shows no strong evidence of a spectral cutoff. An investigation into correlations between the multiwavelength observations found evidence of optical and gamma-ray correlations, suggesting a single-zone model of emission. Finally, the multiwavelength spectral energy distribution is well described by a simple one-zone leptonic synchrotron self-Compton radiation model.

*Unified Astronomy Thesaurus concepts:* Gamma-rays (637); High energy astrophysics (739); Blazars (164); Active galactic nuclei (16); Jets (870)

## 1. Introduction

The extragalactic gamma-ray sky is dominated by blazars (Dermer & Giebels 2016), a subclass of radio-loud active galactic nuclei (AGNs) powered by a central supermassive black hole (SMBH) that display relativistic jets pointed close to Earth. Blazars are characterized by nonthermal continuum emission spanning the entire electromagnetic spectrum and by very fast variability that has been observed down to timescales of minutes in the very high energy (VHE, $E_\gamma \geqslant 100$ GeV) regime (Gaidos et al. 1996; Albert et al. 2007; Aharonian et al. 2009; Abeysekara et al. 2020).

The spectral energy distribution (SED) of blazars typically displays two broad emission features. The first one, in the radio to X-ray wave band, is commonly attributed to synchrotron emission from relativistic electrons and positrons in the jet. The origin of the second feature, in the X-ray to gamma-ray band, is less clear, and two main scenarios have been postulated to explain it. In leptonic models, the emission is attributed to inverse Compton (IC) scattering between the energetic leptons in the jet and a field of low-energy photons (e.g., Jones et al. 1974; Sikora et al. 1994), either the same synchrotron photons (synchrotron self-Compton (SSC) model) or from an external source (external IC (EIC) model) such as the accretion disk, the broad-line region (BLR), or the molecular torus (MT). In hadronic scenarios, the high-energy photons are produced in cosmic-ray interactions through the decay of neutral pions (e.g., Mannheim & Biermann 1992) or proton synchrotron emission (e.g., Aharonian 2002).

The strong radio source S3 1227+25 (Pauliny-Toth & Kellermann 1972), also known as ON 246 (Dixon & Kraus 1968), was first identified as a candidate BL Lacertae (BL Lac) object in a correlation study between the ROSAT All-Sky Survey and the Hamburg Quasar Survey (Bade et al. 1994), which selected sources with strong X-ray to optical flux ratios. BL Lacs, a subclass of blazars that display weak emission lines, are typically classified as low (LBL), intermediate (IBL), or high (HBL) synchrotron-peaked objects based on the frequency of the synchrotron peak in their SED (Padovani & Giommi 1995; Nieppola et al. 2006; Abdo et al. 2010). Several values are reported in the literature for the synchrotron peak frequency ($\nu_{peak}$) of S3 1227+25: Wu et al. (2009) find a value of $10^{14.11}$ Hz by fitting archival measurements of the synchrotron portion of the SED, while Fan et al. (2016) report $10^{14.42\pm0.13}$ Hz, and the Third Fermi-LAT AGN catalog lists $10^{14.91}$ Hz (Ackermann et al. 2015), placing this source near the boundary between IBL and HBL objects, with only nine IBL objects detected so far in the VHE band.[41]

Radio observations of S3 1227+25 with very long baseline interferometry (Kharb et al. 2008) have resolved a parsec-scale core and jet with apparent bending. The polarization vectors are roughly aligned in the direction of the jet in its inner region, indicating a transverse magnetic field and a sheath of longitudinal magnetic field lines along one of the outer edges of the jet. Lister et al. (2021) have reported a maximum proper motion in the jet of $0.45 \pm 0.04$ mas yr$^{-1}$, which translates into an apparent speed of $\sim 4c$ assuming a redshift $z = 0.135$ (Nass et al. 1996), although the redshift of the source is uncertain.

Nass et al. (1996) report a redshift $z = 0.135$, and this value has been cited in most catalogs that include S3 1227+25 (e.g., Ackermann et al. 2015; Goldoni 2021). However, Nass et al. (1996) do not show a spectrum for S3 1227+25, and for objects where they do not show a new spectrum, they use the spectral results from Bade et al. (1994). Bade et al. (1994) show a featureless spectrum for S3 1227+25 but have another object with absorption lines from the host galaxy at redshift $z = 0.135$, RX J11365+6737. Table 3 of Nass et al. (1996) includes both S3 1227+25, with redshift $z = 0.135$, and RX J11365+6737, with no redshift. We conclude that this is a typographical error in the table and that the redshift of RX J11365+6737 was entered in the wrong row. Neither Nass et al. (1996) nor Bade et al. (1994) show a spectrum from which the redshift of S3 1227+25 can be determined. We obtained new spectroscopy of S3 1227+25 on 2016 February 12 (MJD 57430) using the Kast double spectrograph on the 3 m Shane telescope at the Lick Observatory for 30 minutes with red and blue sides covering the 3500–7000 Å wavelength range. The spectrum was dominated by the continuum emission, and no clear indications of the typical features of a host galaxy (such as G band, Ca H and K or continuum break, Mg Ib, or Na ID) were visible.

Other recent spectroscopy (e.g., Massaro et al. 2015; Paiano et al. 2017) has also failed to determine the redshift. Redshift limits, $0.32 \leqslant z \leqslant 1.78$, have been obtained by Shaw et al. (2013) as part of a large spectroscopic survey of BL Lac sources, where the lower limit depends on an assumed absolute magnitude for the host galaxy and the upper limit is determined statistically from the absence of Ly$\alpha$ absorption features. The normalized median spectrum of S3 1227+25, shown in Figure 1, is from the Steward Observatory blazar monitoring program.[42] Also shown for comparison is the normalized spectrum of a typical late-type galaxy. There is good correspondence for features between 3400 and 4500 Å, covering the region around the H and K break. Identifying observed features with Ca II H and K and the G band yielded a redshift of $z = 0.325$. The expected elliptical galaxy Mg Ib feature is hidden in S3 1227+25 by the O2 *B*-

---

[41] http://tevcat2.uchicago.edu/ (accessed on 2023 February 27).

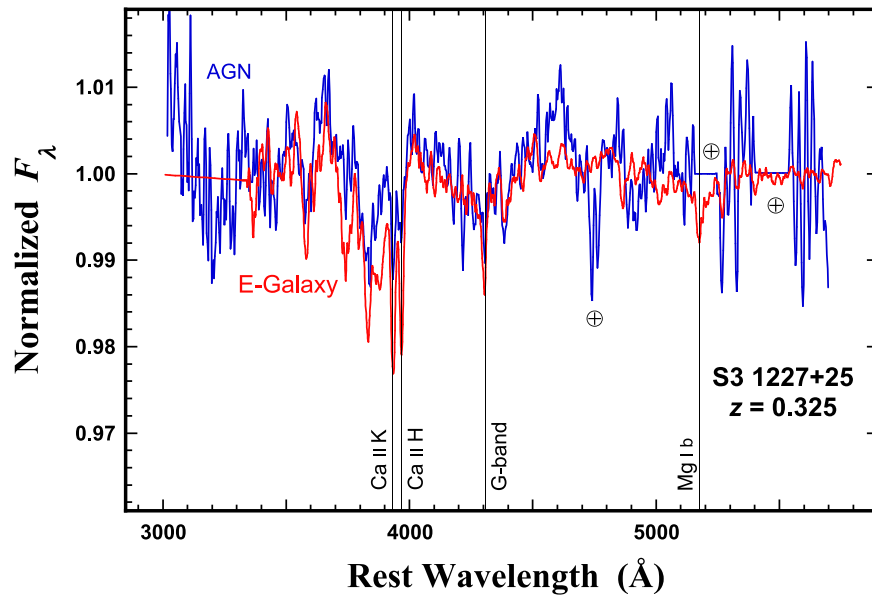[42] Credit: P. S. Smith (in preparation).

**Figure 1.** The normalized median spectrum of S3 1227+25 compared to the normalized spectrum of a typical late-type galaxy. Identifying observed features with Ca II H and K and the G band yielded a redshift of $z = 0.325$. Major telluric absorption features in the spectrum of the AGN are marked with the terrestrial symbol. The redder telluric features have been edited out of the spectrum of S3 1227+25.

band absorption feature. Based on the above discussion, a redshift $z = 0.325$ was assumed for the scientific results presented in this work.

A gamma-ray source positionally consistent with S3 1227 +25 was first identified in Fermi-LAT data and is listed in the Fermi-LAT 1 yr general point-source catalog and subsequent updates, most recently in the 12 yr catalog (4FGL-DR3, Abdollahi et al. 2022). The source was also included in the first Fermi-LAT catalog of sources detected above 10 GeV (1FHL; Ackermann et al. 2013), although it was not identified as a potential VHE emitter given its low flux (about 1% of the Crab Nebula flux above 10 GeV) and a relatively soft, albeit uncertain, spectral index, $\Gamma_{1FHL} = 3.29 \pm 0.95$. While the blazar was not listed in the second catalog of Fermi-LAT sources detected above 50 GeV (2FHL; Ackermann et al. 2016a), it was included in the third Fermi-LAT catalog of sources significantly detected in the 10 GeV–2 TeV energy range (3FHL; Ajello et al. 2017), with a spectral index $\Gamma_{3FHL} = 2.69 \pm 0.22$. Since its first detection, several hard-spectrum GeV flares from S3 1227+25 have been observed with the Fermi-LAT (Becerra 2015; Cutini & Gasparrini 2015).

This work reports the follow-up to the discovery of VHE emission from S3 1227+25 with VERITAS (Mukherjee 2015), based on observations initiated on 2015 May 16 UTC (MJD 57158), following the detection of a strong, hard-spectrum flare of the source with the Fermi-LAT on May 15. The VERITAS detection triggered target-of-opportunity (ToO) observations with Swift, optical photometry, polarimetry, and radio measurements, which are also presented. In particular, we aim to constrain the characteristics and location of the emission region using the large photon statistics during the VHE detection period. In Section 2 we discuss the observations and data analysis routines, from high to low frequencies (VERITAS, Fermi-LAT, X-ray observations, optical telescope data, and radio observations). In Section 3 we describe the methods used to constrain the size and location of the emission region during the VHE detection period. We summarize our conclusions in Section 4.

## 2. Observations and Data Analysis

### 2.1. VERITAS

The Very Energetic Radiation Imaging Telescope Array System (VERITAS) is an array of four 12 m imaging atmospheric Cherenkov telescopes (IACTs) located at the Fred Lawrence Whipple Observatory (FLWO) in southern Arizona, USA (30° 40′ N, 110° 57′ W, 1.3 km above sea level; Holder 2011). Each telescope is equipped with a camera containing 499 photomultiplier tubes, covering a field of view of 3.5°, and is capable of detecting gamma-rays having energies from 85 GeV to above 30 TeV, with an energy resolution of $\Delta E/E \sim 15\%$ (at 1 TeV) and an angular resolution of $\sim0°.1$ (68% containment at 1 TeV). In its current configuration, VERITAS typically detects a source with a flux of 1% of the steady-state gamma-ray flux of the Crab Nebula, at a statistical significance of $>5\sigma$, in 25 hr of observation. It should be noted that the required time to reach a $5\sigma$ detection is longer for sources with a spectrum softer than the Crab Nebula (photon index, $\Gamma > 2.49$) or those observed at large zenith angles ($\theta_z > 40°$; Park & VERITAS Collaboration 2015).

VERITAS observations of S3 1227+25 were started on 2015 May 16 UTC (MJD 57158), following the report of a hard-spectrum GeV flare with the Fermi-LAT. The source was observed for 6.9 hr between May 16 and May 23 (MJD 57158– MJD 57165), at an average zenith angle of 14°, with bad weather conditions at the VERITAS site occasionally preventing observations during this period. The observations were performed using a standard "wobble" observation mode (Fomin et al. 1994) with a 0°.5 offset in each of the four cardinal directions to allow for a simultaneous determination of the background event rate. Quality cuts were applied to the data set to remove observation periods affected by bad weather. The VERITAS data were analyzed using the Eventdisplay analysis package (Maier & Holder 2017) and independently confirmed with the VEGAS analysis package (Cogan 2008), yielding consistent results.
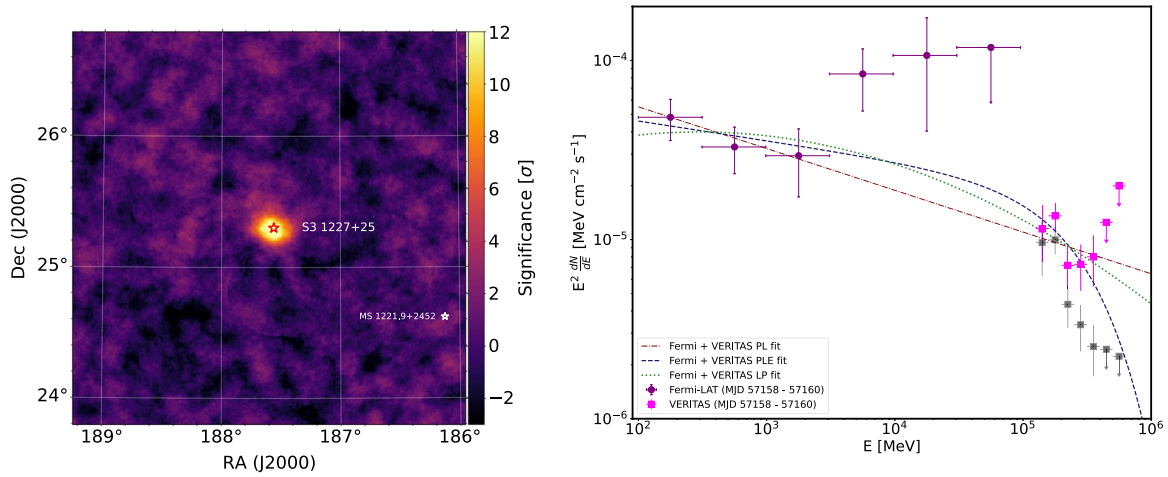
**Figure 2.** Left: VERITAS significance sky map based on observations taken on 2015 May 16 and 2015 May 18 UTC (MJD 57158 and 57160) at the location of the new VHE source positionally coincident with S3 1227+25. The known VHE blazar MS 1221.9+2452, shown with a white marker, was not detected during this period. Right: the purple data points show the Fermi-LAT spectrum obtained for S3 1227+25 in the energy range 100 MeV–100 GeV between 2015 May 16 and May 18 UTC (MJD 57158–57160). The data are binned into two energy bins per decade, with individual bins having a TS < 4 (roughly corresponding to a significance of ~2σ) considered as upper limits. The magenta data points show the VHE spectrum for S3 1227+25 based on VERITAS observations taken on 2015 May 16 and May 18 UTC (MJD 57158–57160). A minimum significance of two standard deviations and three on-source photons are required for each flux point, and upper limits at 95% confidence level are quoted otherwise. De-absorbed flux points, using the Domínguez et al. (2011) EBL model, are shown in magenta, and the corresponding observed fluxes are shown in black. Functions for power law (PL), power law with exponential cutoff (PLE), and log parabola (LP) are fit to the de-absorbed combined gamma-ray spectrum and are shown as dashed red, blue, and green curves, respectively.

The VERITAS analysis parameterizes the principal moments of the elliptical shower images and applies a set of cuts to these parameters to reject cosmic-ray background events. The cuts are determined using a boosted decision tree algorithm (Krause et al. 2017), previously trained on gamma-ray shower simulations and optimized for soft-spectrum sources ($\Gamma \sim 4$). Only events with at least two telescope images are selected during this process. Gamma-ray candidate events are considered to fall in the source (ON) region if the squared angular distance, $\theta^2$, between the reconstructed event origin and S3 1227+25 is less than 0.008 deg$^2$. The background is estimated using the reflected region model (Berge et al. 2007), where circular regions with the same size as the ON region are placed at the same radial distance from the center of the camera. The source was detected on two separate nights, May 16 (MJD 57158) and May 18 (MJD 57160), during which a total of 4.9 hr of observations were obtained. Bad weather meant that S3 1227+25 could not be observed with VERITAS on May 17 (MJD 57159).

An excess of 193 gamma-ray candidate events were recorded in the source region with $N_{\mathrm{ON}} = 333$ ON events, $N_{\mathrm{OFF}} = 1164$ OFF events, a background normalization factor $\alpha = 0.12$, and $N_{\mathrm{Excess}} = N_{\mathrm{ON}} - \alpha N_{\mathrm{OFF}} = 193$, corresponding to a statistical significance of 12.7σ, calculated following the method of Li & Ma (1983). The background normalization factor, $\alpha$, is defined as the ratio of the on-source exposure to the background exposure and accounts for differences, for example, in solid angle, exposure time, zenith angle, and the detector acceptance for gamma-ray-like cosmic-ray events between the ON region and the background region (Berge et al. 2007). A significance sky map centered on the position of S3 1227+25 is shown in Figure 2. The excess event map was fit with a two-dimensional Gaussian function to determine the source centroid, found at a distance of $1'.3 \pm 0'.4_{\mathrm{stat}} \pm 0'.8_{\mathrm{sys}}$ from the VLBA location of S3 1227+25, $\alpha_{2000} = 12^{\mathrm{h}} 30' 14''.09$ and $\delta_{2000} = +25° 18' 7''.14$ (Beasley et al. 2002), within statistical and systematic uncertainties. S3 1227+25 is therefore assigned the VERITAS catalog name VER J1230+253.

The differential energy spectrum, shown in Figure 2, was derived using observations on May 16 and May 18 (MJD 57158–MJD 57160) and fit with a power-law (PL) function of the form $dN/dE = I_0(E/E_0)^{-\Gamma}$, where $E_0 = 0.2$ TeV. A good fit ($\chi^2/\mathrm{ndf} = 2.6/3$) is found for a flux normalization $I_0 = (1.61 \pm 0.19_{\mathrm{stat}}) \times 10^{-10}$ cm$^{-2}$ s$^{-1}$ TeV$^{-1}$ and a spectral index $\Gamma = 3.79 \pm 0.40_{\mathrm{stat}}$. The average integral flux above 0.12 TeV during the two nights was $(4.51 \pm 0.44) \times 10^{-11}$ cm$^{-2}$ s$^{-1}$, or 8.9% of the Crab Nebula flux above the same energy threshold. Furthermore, while observations on May 19, 20, and 23 (MJD 57161, 57162, and 57165, respectively) did not yield a detection, 95% confidence level upper limits on the gamma-ray flux of the source were derived during those periods. A light curve of the VERITAS flux above a threshold of 120 GeV and binned in daily intervals is shown in Figure 3. Finally, we found no evidence of intranight variability in the VERITAS data, as a light curve for observations taken on May 16 and May 18, binned in 4-minute intervals, was found to be well fit by a constant function, with a $\chi^2/\mathrm{dof} = 0.76$, indicating that a constant flux is consistent with the data given the statistical uncertainties.

### 2.2. Fermi-LAT

The Fermi Large Area Telescope (LAT; Atwood et al. 2009) is a pair conversion telescope capable of detecting gamma-ray photons in the energy range from 20 MeV to above 500 GeV. Primarily operating in survey mode, the Fermi-LAT scans the entire sky every 3 hr. In this work, we analyzed Fermi-LAT photons detected between MJD 57128 and MJD 57189, which corresponds to midnight on 2015 April 16 until midnight on 2015 June 16, a month on either side of the VERITAS detection (Mukherjee 2015). Throughout the analysis, we use the Fermi Science Tools version 11 − 05 − 03,[43] FERMIPY version 1.0.1[44] (Wood et al. 2017), in conjunction with the

---

[43] http://fermi.gsfc.nasa.gov/ssc/data/analysis/software (accessed on 2023 February 27).
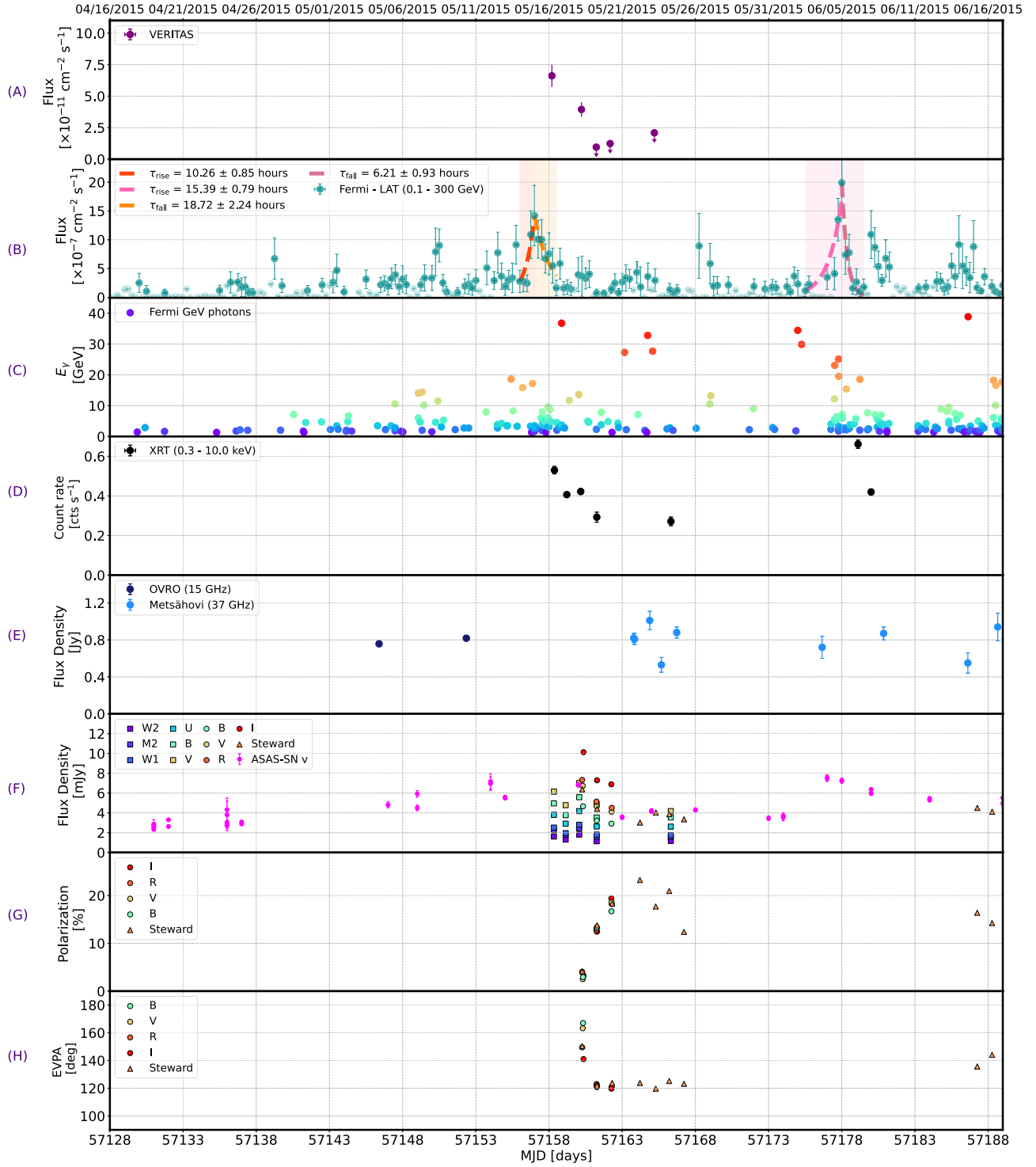[44] http://fermipy.readthedocs.io (accessed on 2023 February 27).

**Figure 3.** Multiwavelength light curves of S3 1227+25 between MJD 57128 and MJD 57189, which corresponds to midnight on 2015 April 16 until midnight on 2015 June 16, a month on either side of the VERITAS detection. (a) Daily binned VHE light curve for VERITAS observations above an energy threshold of 120 GeV. Upper limits at 95% confidence level are quoted for observations with a significance of lower than $2\sigma$. (b) Fermi-LAT light curve in 6 hr bins in the 0.1–300 GeV band. The shaded regions indicate the two periods of flaring activity used to compute the variability timescales, obtained from the fits (dashed curves) and shown in the legend. Upper limits are shown for individual bins having a significance of lower than $2\sigma$. (c) Fermi-LAT GeV photon energies positionally coincident (at 95% containment) with the source position. (d) Swift-XRT count rate in the 0.3–10 keV band. (e) Radio flux observations: OVRO (dark blue) and Metsähovi (light blue) light curves at 15 and 37 GHz, respectively. (f) Optical/UV flux observations: Swift-UVOT (squares), Lowell Observatory (circles), Steward photometry in the 4000–7000 Å band (triangles), and optical data, not corrected for extinction, from the ASAS-SN Sky Patrol (magenta points). (g) Electric vector polarization angle (EVPA): Lowell Observatory (circles), Steward photometry in the 4000–7000 Å band (triangles). (h) Polarization: Lowell Observatory (circles), and Steward photometry in the 4000–7000 Å band (triangles).

latest PASS 8 instrument response functions (IRFs) (Atwood et al. 2013).

Photons with energies between 100 MeV and 100 GeV that were detected within a region of interest (ROI) of radius 15° centered on the location of S3 1227+25 were selected for the analysis. Furthermore, we selected only photon events from within a maximum zenith angle of 90° in order to reduce contamination from background photons from Earth's limb, produced from the interaction of cosmic-rays with the upper atmosphere.

The contributions from the isotropic and Galactic diffuse backgrounds were modeled using the most recent templates for isotropic and Galactic diffuse emission, iso_P8R3_SOURCE_V2_v1.txt and gll_iem_v07.fits, respectively. Sources in the 4FGL-DR3 catalog within a radius of 20° from the source position of S3 1227+25 were included in the model, with their spectral parameters fixed to their catalog values. This takes into account the gamma-ray emission from sources lying outside the ROI, which might yet contribute photons to the data, especially at low energies, due to the size of the point-spread function of the Fermi-LAT.

The normalization factors for both the isotropic and Galactic diffuse emission templates were left free along with the spectral normalization of all modeled sources within the ROI. Moreover, the spectral shape parameters of all modeled sources within 3° of S3 1227+25 were left free to vary, while those of the remaining sources were fixed to the values reported in the 4FGL-DR3 catalog (Abdollahi et al. 2022). A binned likelihood analysis was then performed in order to obtain the spectral parameters best describing the model during the period of observation, using a spatial binning of 0.1° pixel$^{-1}$ and two energy bins per decade.

The source was detected at a high statistical significance of more than $49\sigma$ (TS = 2476.7) during the observation period analyzed. The spectrum was found to be best modeled by a log parabola (LP):

$$\frac{dN}{dE} = N_0 \left(\frac{E}{E_0}\right)^{-\alpha - \beta \ln\left(\frac{E}{E_0}\right)},\qquad(1)$$

where $N_0$ is the normalization, $E_0$ is the pivot energy, $\alpha$ is the spectral index, and $\beta$ is the curvature. The best-fit spectral parameters obtained for S3 1227+25 during the period investigated are $N_0 = (5.04 \pm 0.27) \times 10^{-11}$ cm$^{-2}$ s$^{-1}$ MeV$^{-1}$, $\alpha = 1.85 \pm 0.05$, and $\beta = 0.05 \pm 0.02$. For comparison, the 4FGL-DR3 catalog spectral values for this source are $N_0 = (7.21 \pm 0.16) \times 10^{-12}$ cm$^{-2}$ s$^{-1}$ MeV$^{-1}$, $\alpha = 2.02 \pm 0.02$, and $\beta = 0.06 \pm 0.01$.

The differential energy spectrum, shown in Figure 2, was derived using Fermi-LAT observations between 2015 May 16 and May 18 (MJD 57158–57160). This spectrum was not fitted with an LP model, shown in Equation (1), due to a physically unrealistic negative value obtained for the spectral curvature, $\beta$, and instead we chose to model it using a simple PL model of the form $\frac{dN}{dE} = N_0\left(\frac{E}{E_0}\right)^{-\gamma}$. The best-fit spectral parameters are the normalization $N_0 = (6.52 \pm 1.12) \times 10^{-11}$ cm$^{-2}$ s$^{-1}$ MeV$^{-1}$ and spectral index $\gamma = 1.79 \pm 0.14$. A light curve of the integral flux above 100 MeV, shown in Figure 3, is calculated with 6 hr bins and keeping the spectral index fixed.

Furthermore, we investigated the GeV photon emission from S3 1227+25 for the time interval corresponding to the VERITAS detection. For the purpose of this study, GeV photons are defined as photons having an energy $E_\gamma \geqslant 1$ GeV in the rest frame of the host galaxy. The Fermi science tool *gtsrcprob* estimates the probability of each photon being associated with each source in the ROI and was used to check that the GeV photons detected are associated with S3 1227+25. Before this step, it was necessary to first account for the diffuse components using the Fermi science tool *gtdiffrsp*, and the response was added to the input data.

Figure 3(c) shows the GeV photons emitted from within a radius of 0°.1 around S3 1227+25 and having a $\geqslant$95% probability of originating from it. While the most energetic photon from S3 1227+25 during the period investigated, having energy $33.4 \pm 2.1$ GeV, was emitted on MJD 57186.63 and is outside of the time window of the VERITAS observations, the second most energetic photon, having energy $31.6 \pm 1.9$ GeV, was emitted on MJD 57158.86 and coincides with the VHE discovery.

### 2.3. Swift

The X-Ray Telescope (XRT) on the Neil Gehrels Swift Observatory is a grazing-incidence focusing X-ray telescope, capable of detecting photons in the energy range between 0.2 and 10 keV (Gehrels 2004; Burrows et al. 2005). ToO observations of S3 1227+25 were performed with the Swift-XRT between MJD 57158 and MJD 57180, which corresponds to midnight on May 16 until midnight on 2015 June 7 UTC, in coordination with the VERITAS observations. A total observing time of 16.2 ks was accumulated during this period in photon-counting mode, and the data were analyzed using the HEASOFT v6.21 package.

The average photon count rate from the source in the 0.3–10 keV range for these observations was $0.42 \pm 0.14$ counts s$^{-1}$. Photon pileup at this rate level is negligible, and statistical uncertainties dominate over systematic ones. Photons were binned in energy, and the resulting histogram was fit with an absorbed PL spectrum assuming a Galactic column density of $N_H = 1.43 \times 10^{20}$ cm$^{-2}$. A good fit ($\chi^2$/ndf = 39.4/40) is found for a PL normalization of $(2.73 \pm 0.09) \times 10^{-3}$ keV$^{-1}$ s$^{-1}$ at 1 keV and a photon index of $2.35 \pm 0.06$. A light curve of the absorption-corrected flux values is shown in Figure 3, and the data are also used in the modeling of the broadband SED of the source in Section 3.4.

The Ultraviolet/Optical Telescope (UVOT) on the Neil Gehrels Swift Observatory is a photon-counting telescope. It is sensitive to photons with energies ranging roughly between 1.9 and 7.3 eV (Roming et al. 2005). Swift-UVOT observations in the optical−UV band are performed in parallel to XRT measurements. Swift-UVOT observations in the *UW1*, *UW2*, *UM2*, *U*, *B*, and *V* band filters were analyzed using the `uvotsource` routine by selecting source photons from a circular region of radius 5″ centered on S3 1227+25 and estimating the background in a 30″-radius circular region away from the blazar and containing no obvious sources in any band. The measured optical−UV fluxes are shown in Figure 3 after correcting for interstellar extinction using the approach of Roming et al. (2009), assuming a reddening of $E(B - V) = 0.0167$ (Schlafly & Finkbeiner 2011).

### 2.4. Optical

S3 1227+25 was observed with the 1.8 m Perkins telescope at the Lowell Observatory and the 1.6 m Kuiper and 2.3 m Bok telescopes at the Steward Observatory in Arizona between 2015 May and July. As seen in Figure 3, a low degree of polarization is observed in both data sets on the first night of observations. Observations and data reductions were performed in the same manner as described in Jorstad et al. (2010) and Smith et al. (2009). The spectroscopic observations performed at Steward Observatory show no variation in the slope of the flux spectrum during the active period. Furthermore, S3 1227 +25 is known to be highly variable at optical wavelengths, with the flux density ranging from 14 to 16 mag in the R band and the degree of polarization ranging between 3% and 25% according to the optical monitoring at the Perkins telescope in Flagstaff, Arizona, USA.

The All-Sky Automated Survey for Supernovae (ASAS-SN; Shappee et al. 2014; Kochanek et al. 2017) is an automated program aimed at routinely surveying the entire visible sky for bright transient sources with minimal observational bias and reaches a depth of roughly 17 mag. ASAS-SN originally consisted of two stations, located at the Cerro Tololo International Observatory (CTIO, Chile) and the Haleakala Observatory (Hawaii). In 2017, three further stations were added, including a second unit at CTIO and one unit each at the McDonald Observatory (Texas) and the South African Astrophysical Observatory.

The observations made with ASAS-SN are available in two optical bands: the $v$ band, centered at $\sim$551 nm and corresponding to observations from the two original stations, and the $g$ band, centered at $\sim$480 nm and corresponding to observations performed with the three new stations. For the purpose of this study, we obtain S3 1227+25 observations with ASAS-SN from the ASAS-SN Sky Patrol[45] for the time interval between MJD 57128 and MJD 57189, corresponding to midnight on 2015 April 16 until midnight on 2015 June 16 UTC, a month on either side of the VERITAS detection.

The Asteroid Terrestrial-impact Last Alert System (ATLAS; Tonry et al. 2018) is a high-cadence all-sky survey system comprising two independent units, one on Haleakala (HKO) and one on Mauna Loa (MLO) in the Hawaiian islands. ATLAS was optimized to be an efficient system for finding potentially dangerous asteroids, as well as tracking and searching for variable and transient sources. It is capable of discovering more bright (less than 19 mag) supernova candidates than other ground-based surveys. For the purpose of this study, we obtain S3 1227+25 observations with ATLAS in the R band, centered at 679 nm, having a typical cadence of one data point per 2 days, shown in Figure 4.

### 2.5. Radio

Radio observations of S3 1227+25 at 15 GHz were routinely performed at a few-days cadence as part of the Owens Valley Radio Observatory (OVRO) Fermi-LAT blazar monitoring program (Richards et al. 2011), and the light curve around the VERITAS detection is shown in Figure 3. The long-term light curve for the source, shown in Figure 4, indicates that the blazar reached historically high flux levels around the time of the VHE detection.

Due to hardware issues, the monitoring was interrupted during the period surrounding the flare, with the last flux data point taken on MJD 57152 (5 days before the Fermi-LAT GeV flare detection and 6 days before the VERITAS one), and observations resumed on MJD 57229. The flux value recorded on MJD 57152 is used in the modeling of the broadband SED of the source in Section 3.4, where the uncertainty on the value represents the range of fluxes measured 100 days around the date of the first VHE detection (MJD 57158).

Figures 3 and 4 show the 37 GHz observations of S3 1227 +25 performed at the Metsähovi Radio Observatory with the 13.7 m radio telescope. This is located in Finland and at 37 GHz has a detection limit of the order of 0.2 Jy under optimal conditions. The typical integration time required to obtain a single flux density point is between 1200 and 1800 s, and data points having a signal-to-noise ratio of less than 4 are considered as nondetections and shown as upper limits. The flux density scale is set by observations of the H II region DR21 with the sources NGC 7027, 3C 274, and 3C 84 used as secondary calibrators. A detailed study of the methods used in the data analysis is found in Teraesranta et al. (1998).

## 3. Results

### 3.1. Temporal Variability

Localizing the gamma-ray emission region in blazars is an indirect process with a variety of different methods previously used in the literature. The observation of rapid flux variability in these sources implies that the emission is coming from compact regions. Blazars have been found to show variability at timescales down to the order of a few minutes in both GeV and TeV bands, for example, PKS 2155−304 (Aharonian et al. 2009), 3C 279 (Ackermann et al. 2016b), and Mrk 421 (Abeysekara et al. 2020). It should be noted that compact emission regions do not automatically imply emission from near the SMBH, as overdensities of the plasma can occur throughout the jet, including within the MT region. It has been proposed that these result from magnetic reconnection events (Giannios et al. 2009; Giannios 2013), the recollimation of the jet (Bromberg & Levinson 2009), or turbulence in the jet (Marscher & Jorstad 2021).

The temporal gamma-ray variability of S3 1227+25 during the VERITAS detection was quantified by calculating the time taken for the flux to increase or decrease by a factor of 2. Known as the doubling or halving timescale, $\tau$, this is defined as

$$F(t) = F(t_0)\, 2^{\tau^{-1}(t-t_0)}, \qquad (2)$$

where $F(t)$ and $F(t_0)$ are the fluxes at times $t$ and $t_0$, respectively. The measurement of doubling timescales is frequently used in the study of blazars (e.g., Foschini et al. 2011; Saito et al. 2013), and applying the same method allows for comparability. A least-squares fitting routine to Equation (2) was applied to time intervals corresponding to flaring episodes in the 6 hr binned Fermi-LAT light curve, shown in Figure 3.

There is no general consensus on how to define a flaring episode (e.g., Resconi et al. 2009; Meyer et al. 2019). Nalewajko (2013) defines flares as a contiguous interval of time containing a flux peak, having a flux higher than half the peak value of the entire observation. Meyer et al. (2019) adopt a simple two-step procedure for identifying blocks of data
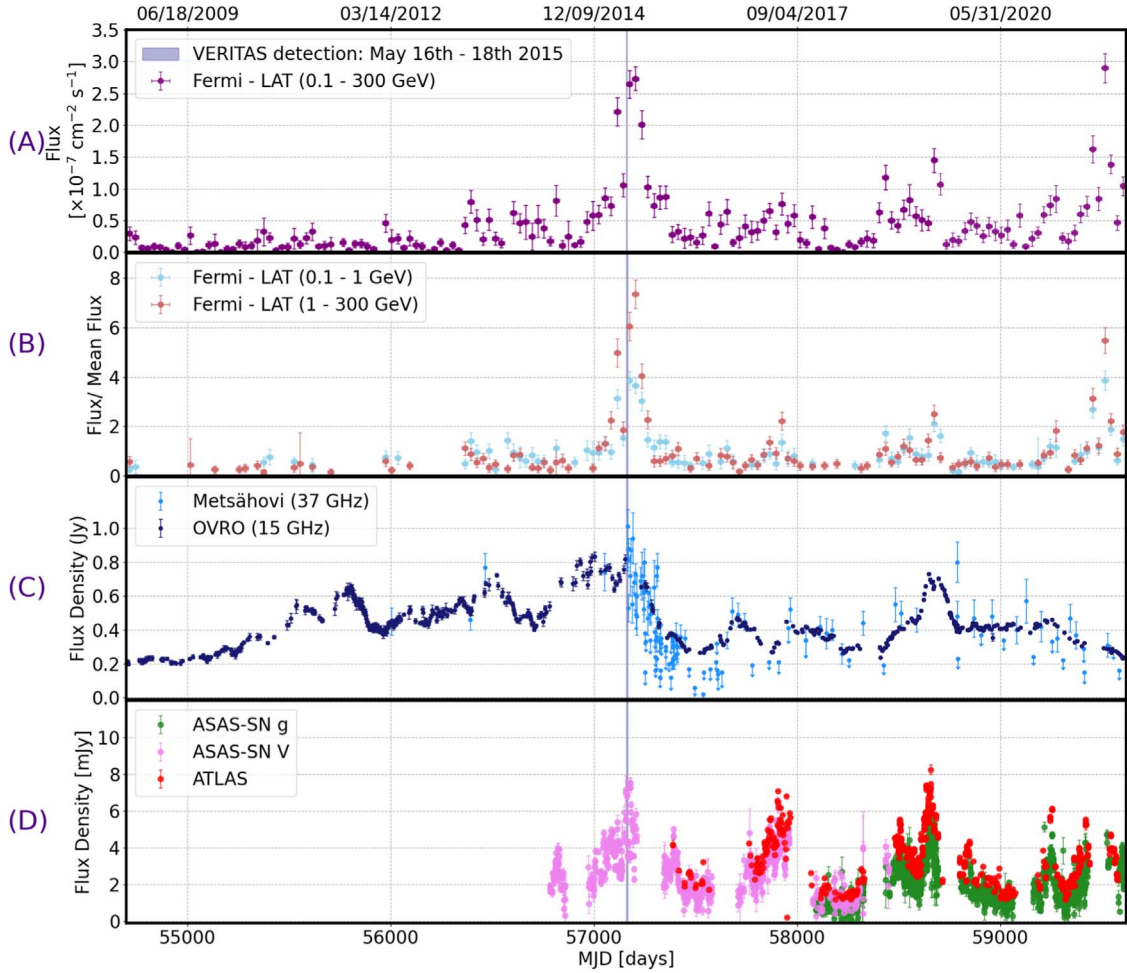
---

**Figure 4.** Multiwavelength light curves of S3 1227+25 over a wider time interval, MJD 54683 to MJD 59611, corresponding to midnight on 2008 August 4 until midnight on 2022 February 1. The blue narrow band corresponds to the VERITAS detection. (a) Fermi-LAT light curve in the 0.1–300 GeV band. (b) Separate Fermi-LAT light curves showing the low-energy flux (0.1 GeV $\leqslant E_\gamma \leqslant$ 1 GeV) as blue circles and the high-energy flux (1 GeV $\leqslant E_\gamma \leqslant$ 300 GeV) as red circles. To aid visual comparison, the individual flux values have been divided by the mean flux in the corresponding energy ranges. The error bars are purely statistical, and only data points with TS $\geqslant$ 10 are shown. (c) Radio flux observations: OVRO (dark blue) and Metsähovi (light blue) light curves at 15 and 37 GHz, respectively. For the Metsähovi data, individual bins having a signal-to-noise ratio of less than 4 are considered nondetections and shown as upper limits. (d) Optical flux observations: optical data, not corrected for extinction, from the ASAS-SN Sky Patrol in the g and V band (green and magenta, respectively), and ATLAS R-band data (in red).

points, having a flux higher than both the preceding and subsequent blocks and proceeding in both directions, as long as the blocks have successively lower fluxes. In this study, we define a flare using the method described in Acharyya et al. (2021), which combines these two approaches. We identify local peaks in flux, defined as bins having a higher flux than both the preceding and succeeding bins. We then proceed in both directions, as long as the corresponding bins have, within errors, successively lower or compatible fluxes. We also impose the condition that the peak of the flare must, within errors, have a flux greater than twice the average flux during the entire observation period (i.e., $F_{\mathrm{peak}} - \Delta F_{\mathrm{peak}} \geqslant 2^* F_{\mathrm{mean}}$). Also shown in Figure 3 are the two time periods satisfying our definition of a flare and used to compute the variability timescales.

The fastest observed variability timescale is found to be $\tau_{\mathrm{obs}} = 6.2 \pm 0.9$ hr. This corresponds to the time interval between $t_0 = $ MJD 57178 and $t = $ MJD 57179.5, where the flux decreased from $F(t_0) = (19.9 \pm 5.2) \times 10^{-7}$ photons cm$^{-2}$ s$^{-1}$ to $F(t) = (1.8 \pm 0.9) \times 10^{-7}$ photons cm$^{-2}$ s$^{-1}$. Using geometric arguments, the shortest observed variability timescale

was used to constrain the size of the emission region:

$$r \leqslant \frac{c\delta\tau_{\mathrm{obs}}}{1 + z}, \tag{3}$$

where $r$ is the size of the emission region, $c$ is the speed of light, the Doppler factor of the jet $\delta = 9.6$ (Zhou et al. 2021), and the redshift of the source $z = 0.325$. The measured fastest observed variability timescale, $\tau_{\mathrm{obs}} = 6.2 \pm 0.9$ hr, corresponds to a gamma-ray emission region of size $r \leqslant (6.4 \pm 0.9) \times 10^{13}$ m. It should be noted that the Doppler factor of the jet, $\delta = 9.6$, measured in Zhou et al. (2021) is obtained from archival SEDs, which may not be contemporaneous data sets, and a variability timescale in the host frame of 1 day is considered for all sources, with the Doppler factor assumed to be equal to the Lorentz factor.

### 3.2. Gamma-Ray Spectrum

Regions near the central engine of AGNs are photon-rich environments, and the interactions between these photons and gamma-ray photons result in photon−photon pair production

**Table 1**
Best-fit Spectral Parameters Obtained from a Joint Fit to the Combined Gamma-Ray Spectrum for S3 1227+25, Observed with the Fermi-LAT and VERITAS between 2015 May 16 and May 18 UTC (MJD 57158–57160), Using PL, PLE, and LP Functions

| Fit Function | $N_0$ $(10^{-12}\ \mathrm{cm}^{-2}\ \mathrm{s}^{-1}\ \mathrm{MeV}^{-1})$ | $\alpha$ | $\beta$ | $E_0$ (MeV) | $E_{\mathrm{cut}}$ (GeV) | $\chi^2/\mathrm{dof}$ | AIC |
|---|---|---|---|---|---|---|---|
| PL | $24.8 \pm 4.3$ | $2.23 \pm 0.04$ | $\cdots$ | 816 | $\cdots$ | 1.50 | 6.27 |
| PLE | $28.0 \pm 5.2$ | $2.10 \pm 0.10$ | $\cdots$ | 816 | $282 \pm 203$ | 1.40 | 6.22 |
| LP | $30.2 \pm 7.4$ | $2.07 \pm 0.16$ | $0.04 \pm 0.03$ | 816 | $\cdots$ | 1.53 | 7.19 |

**Note.** The final two columns state the $\chi^2/\mathrm{dof}$ and AIC values obtained for each model.

$(\gamma\gamma \rightarrow e^+e^-)$. The MT has comparatively a much lower photon density than the BLR, meaning that there is less likelihood of pair production within the MT. Pair production manifests itself as an attenuation of the gamma-ray spectrum for emission coming from near the SMBH (Poutanen & Stern 2010; Stern & Poutanen 2014), whereas emission originating from within the MT is not expected to have this spectral feature (Donea & Protheroe 2003; Liu & Bai 2006). It should be noted that the presence of a potential cutoff in the spectrum can also be the consequence of a break in the energy distribution of the emitting electrons (Dermer et al. 2015).

To investigate the spectral attenuation, we corrected the VERITAS and Fermi-LAT flux points for attenuation by extragalactic background light (EBL) using the Domínguez et al. (2011) model and assuming redshift $z = 0.325$. A joint fit was performed to the de-absorbed gamma-ray spectrum for the time interval corresponding to the VERITAS detection and is shown in Figure 2. The combined gamma-ray spectrum was modeled with a simple PL model of the form $\frac{dN}{dE} = N_0\left(\frac{E}{E_0}\right)^{-\alpha}$, a PL function with exponential cutoff (PLE) model of the form $\frac{dN}{dE} = N_0\left(\frac{E}{E_0}\right)^{-\alpha} e^{-\left(\frac{E}{E_{\mathrm{cut}}}\right)}$, and an LP model of the form $\frac{dN}{dE} = N_0\left(\frac{E}{E_0}\right)^{-\alpha - \beta \ln\left(\frac{E}{E_0}\right)}$. Here $N_0$ is the normalization, $\alpha$ is the spectral index, $\beta$ is the spectral curvature, $E_0$ is the pivot energy, and $E_{\mathrm{cut}}$ is the cutoff energy. The best-fit spectral parameters are tabulated in Table 1, along with the $\chi^2/\mathrm{dof}$ obtained for each fit. It should be noted that, despite covering the same time period, the Fermi-LAT and VERITAS spectral data are not strictly contemporaneous.

To compare the fits provided by all three models, an Akaike information criterion (AIC) test (Akaike 1974) was performed. The AIC of a model $s$ is given by $\mathrm{AIC}_s = -2\ln L_s + 2k_{f_s}$, where $L_s$ is the likelihood of the model $s$ and $k_{f_s}$ is the number of free parameters in the model. The difference in AIC values between two models $s$ and $s'$, $\Delta\mathrm{AIC}_{s,s'} = \mathrm{AIC}_s - \mathrm{AIC}_{s'}$, estimates how much more the model $s$ diverges from the true distribution than the model $s'$ (Burnham & Anderson 2001; Harris et al. 2012). A lower AIC value means a better description of the spectrum, and an AIC difference of greater than 2 between two models means that the model with the higher AIC is significantly worse than the model with the lower AIC value (Lewis et al. 2011). The AIC values for the PL, PLE, and LP models are tabulated in Table 1. The combined gamma-ray spectrum was found to favor none of the three models significantly, with $\Delta\mathrm{AIC}_{\mathrm{PL,PLE}} = 0.05$ and $\Delta\mathrm{AIC}_{\mathrm{LP,PLE}} = 0.97$, respectively.

### 3.3. Results from Multiwavelength Correlation Analysis

In SSC models of blazar emission, both synchrotron scattering and IC scattering derive from the same population of electrons, resulting in strong correlations between low- and high-energy wave bands (Sikora et al. 1994). On the other hand, the observation of orphan flares in one wave band having no correlation with others, for example, the 2002 flare of 1ES 1959+650 (Krawczynski et al. 2004), can be interpreted as evidence of multiple emission zones or support for hadronic emission models. Investigating multiwavelength correlations helps in identifying relationships between emission zones and in placing constraints on the dominant mechanisms responsible.

In Figure 3, we present multiwavelength light curves corresponding to the time period around the VERITAS detection. We now consider multiwavelength light curves over a wider time interval, MJD 54683 to MJD 59611, and discuss potential correlations between them. This corresponds to midnight on 2008 August 4, the start of the Fermi-LAT mission, until midnight on 2022 February 1. The light curves considered are presented in Figure 4 and include the Fermi-LAT light curve, obtained using the data reduction routine described in Section 2.2, as well as radio light curves, measured with Metsähovi and OVRO, and optical light curves, obtained from the ASAS-SN Sky Patrol and ATLAS data. There were not sufficient statistics to enable a cross-correlation analysis using the VERITAS and X-ray observations. The Fermi-LAT data are also investigated in two distinct energy ranges, 0.1–1 GeV (low energy) and 1–300 GeV (high energy), binned in daily intervals using the procedure outlined in Section 2.2 and shown in Figure 4.

Local cross-correlation functions (LCCFs; Welsh 1999) are applied to pairs of two different light curves to search for correlations between them. For two light curves having fluxes $a_i$ and $b_j$, corresponding to times $t_{a_i}$ and $t_{b_j}$, the LCCF is computed as

$$\mathrm{LCCF}(\tau) = \frac{1}{M} \frac{\Sigma(a_i - \bar{a}_\tau)(b_j - \bar{b}_\tau)}{\sigma_{a\tau}\sigma_{b\tau}}, \quad (4)$$

where the sums run over M pairs for which $\tau \leqslant t_{a_i} - t_{b_j} < \tau + \Delta t$ for a chosen time step $\Delta t$, $\bar{a}_\tau$ and $\bar{b}_\tau$ are flux averages, and $\sigma_{a\tau}$ and $\sigma_{b\tau}$ are standard deviations over the M pairs, respectively (Welsh 1999). As also adopted in Meyer et al. (2019), for the binning of the time lags, $\tau$, we choose the higher half median of the time separations between consecutive data points in the two light curves. Furthermore, the minimum and maximum values of $\tau$ are chosen to be $\pm 0.5$
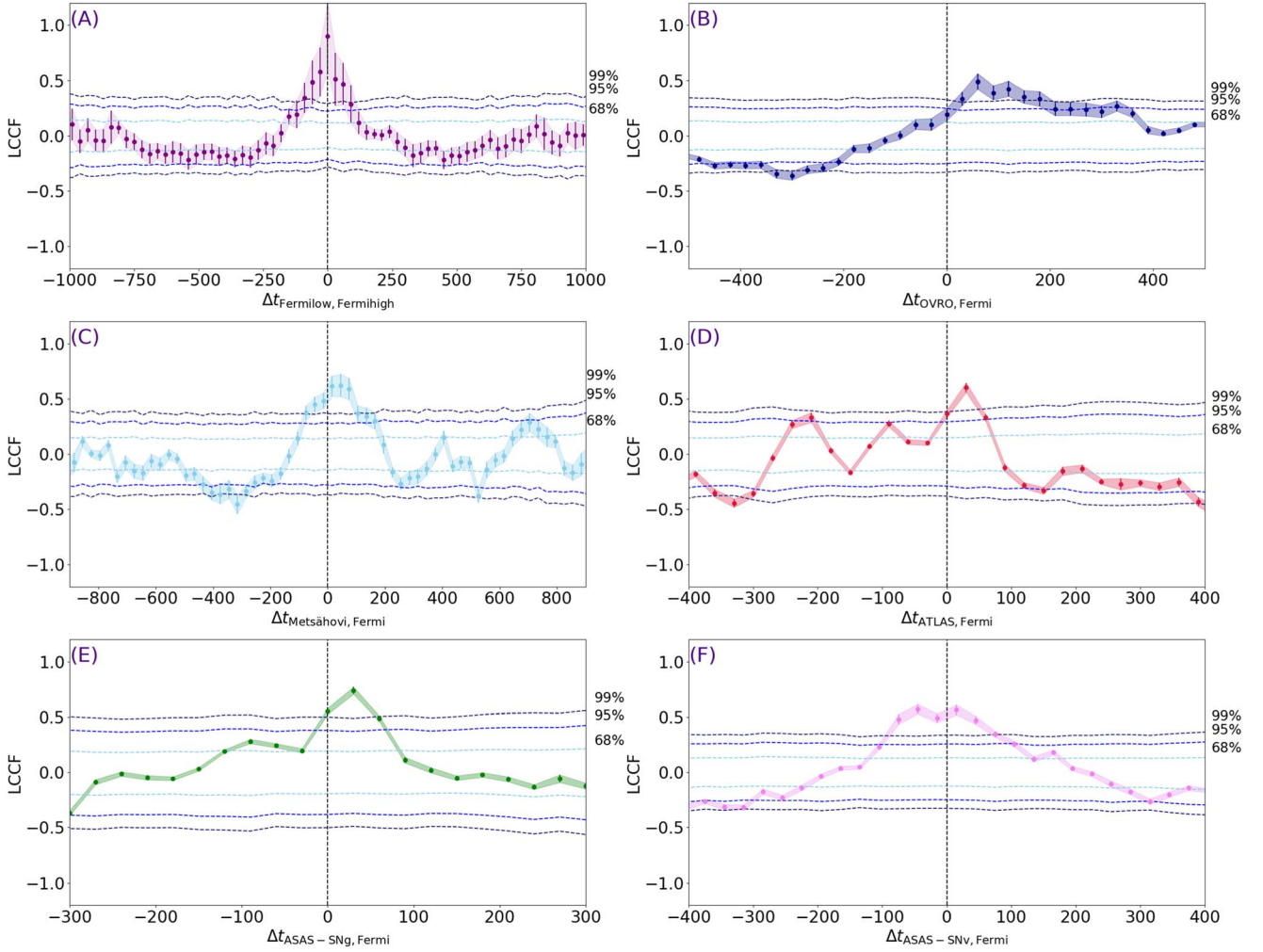
**Figure 5.** LCCFs calculated between the different light curves are shown in color. The x-axis represents the time delay, $\Delta t_{a,b} = t_a - t_b$, in days for two light curves $a$ and $b$. The dashed vertical line corresponds to $\Delta t_{a,b} = 0$. The corresponding shaded regions indicate the error bounds of the LCCFs. The blue lines represent the 68%, 95%, and 99% confidence intervals (from lighter to darker shades) derived from Monte Carlo simulations.

times the length of the shorter light curve (Max-Moerbeck et al. 2014).

The LCCF method is independent of any differences in sampling rates of the two light curves. Furthermore, unlike discrete correlation functions (DCFs; Edelson & Krolik 1988), LCCFs are intrinsically bound in the interval [−1, 1]. Moreover, the use of LCCFs has been found to be more efficient than DCFs in the study of correlations (Max-Moerbeck et al. 2014). The LCCF obtained between the low- and high-energy Fermi-LAT light curves is shown in Figure 5, along with the LCCFs obtained between the full energy range Fermi-LAT light curve and each of the other light curves considered.

Monte Carlo simulations are used to determine the significance of an obtained LCCF value, using 1000 artificial light curves that match the probability distribution function and power spectral density of each observation using the method outlined in Emmanoulopoulos et al. (2013). The 68%, 95%, and 99% confidence intervals obtained are shown in Figure 5. As seen in panel (a) of Figure 5, the Fermi-LAT light curves in the different energy regimes are found to show evidence of a strong correlation with a peak compatible with zero time lag. This can be interpreted as evidence that the MeV and GeV components of the flare have the same origin.

**Table 2**
Best-fit Parameters of a Simple One-zone Synchrotron and SSC Radiation Model Fitted to the Multiwavelength Broadband SED of S3 1227+25 taken between 2015 May 16 and 18 (MJD 57158–57160)

| Parameter | Value |
|---|---|
| $\log_{10}(B\,[\mathrm{G}])$ | $0.10^{+0.03}_{-0.02}$ |
| $\log_{10}(k_e\,[\mathrm{cm}^{-3}])$ | $-2.23^{+0.11}_{-0.12}$ |
| $\log_{10}(\gamma_b)$ | $3.51^{+0.04}_{-0.04}$ |
| $p1$ | $1.40^{+0.41}_{-0.28}$ |
| $p2$ | $3.74^{+0.02}_{-0.02}$ |
| $\delta$ | 9.6 |
| $r\,[10^{13}\,\mathrm{m}]$ | 6.40 |
| $z$ | 0.325 |
| $\gamma_{min}$ | 500 |
| $\gamma_{max}$ | $10^6$ |

**Note.** The parameters $\delta$, $r$, $\gamma_{min}$, $\gamma_{max}$, and $z$ have been kept fixed, while the other parameters are left free during the fitting procedure. The best-fit model is shown in Figure 6.

Panels (b) and (c) of Figure 5 show the correlations between the Fermi-LAT data in the 0.1–300 GeV energy band and the 37 and 15 GHz radio flux densities, as measured with
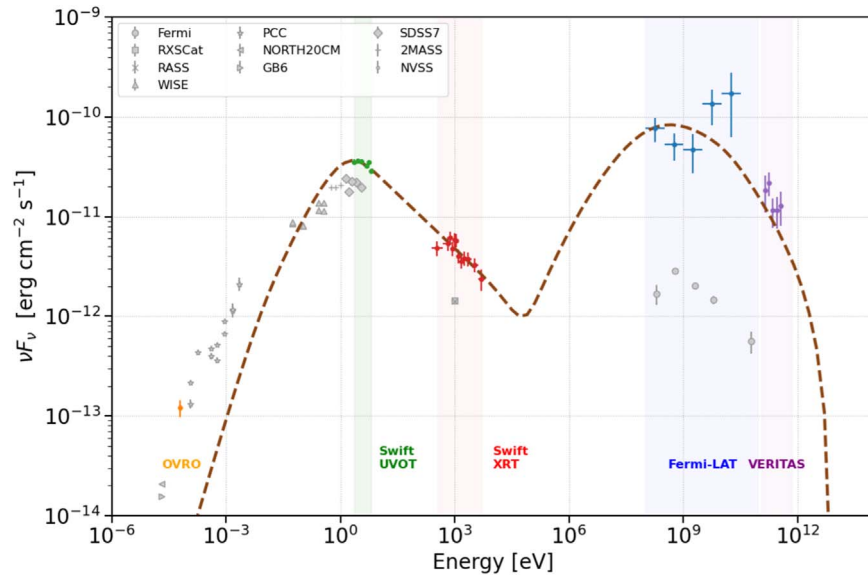
**Figure 6.** The multiwavelength broadband SED of S3 1227+25 during the nights of the VERITAS detection, 2015 May 16–18 (MJD 57158–57160), fitted using *agnpy*. The gray points represent archival data. The dashed brown curve represents the best-fit one-zone synchrotron and SSC radiation model, obtained using all 5000 samples from all 30 walkers, with the parameters shown in Table 2.

Metsähovi and OVRO, respectively. In both cases, a positive correlation is found, significant at a level of above $3\sigma$, and consistent with zero time lag. Moreover, as seen in Figure 4, the radio outburst also started several years earlier than the gamma-ray flare. This could imply that the multiwavelength outburst was built in the jet and the gamma-ray flare and VHE detection were the culmination of it. Furthermore, while we observe visual evidence of a delay between the 37 and 15 GHz radio observations with respect to the Fermi-LAT light curve, it should be noted that the OVRO observations were interrupted during the period surrounding the flare, with the last flux data point taken on MJD 57152 (5 days before the Fermi-LAT GeV flare detection) owing to hardware issues and resuming on MJD 57229. There were not enough data to investigate whether the delay, as seen in the low-state data, is also found during the VHE detection period, and it is not considered for further discussion.

Panels (d), (e), and (f) of Figure 5 show the correlations between the Fermi-LAT data in the 0.1–300 GeV energy range and the optical data taken with ATLAS in the R band and ASAS-SN observations in the *g* and *V* bands, respectively. A positive correlation, significant at a level of above $3\sigma$ and consistent with zero time lag, is seen for correlations between Fermi-LAT data and ATLAS and ASAS-SN *g* data, while we find evidence of a broader peaked correlation, also compatible with a zero lag, for correlations between Fermi-LAT and ASAS-SN *V* observations. The strong optical and gamma-ray correlations found for S3 1227+25 suggest a single-zone model of emission. Under the assumption that the optical and gamma-ray flares are produced by the same outburst propagating down the jet, both positive and negative time lags on timescales of days are predicted in SSC and EIC models (e.g., Sokolov et al. 2004).

### 3.4. SED Modeling

The final method that sheds light on the mechanisms responsible for the VERITAS detection of S3 1227+25 is modeling the multiwavelength SED. In a leptonic scenario, the

second peak in the broadband SED is interpreted as SSC emission or EIC emission (e.g., Maraschi et al. 1992; Sikora et al. 1994). We model the multiwavelength broadband SED of S3 1227+25 taken between 2015 May 16 and May 18 using *agnpy*, an open-source Python package for modeling radiative processes involving relativistic particles accelerated in the jets of AGNs (Nigro et al. 2022). The synchrotron and SSC processes in *agnpy* are based on the work published in Finke et al. (2008) and Dermer & Menon (2009). We assume a 20% systematic uncertainty on the VHE flux measurements, 10% on the Fermi-LAT and X-ray band data, and 5% on the lower-energy UV band. The radio SED point from OVRO was not considered in the fit owing to a larger integration region, contaminated by extended jet emission.

We use a simple one-zone synchrotron and SSC radiation model consisting of a single blob with a broken PL electron energy density (EED). This scenario is most commonly considered to model BL Lacs like S3 1227+25. It consists of nine parameters, including three describing the blob, namely the Doppler factor $\delta$, the magnetic field $B$, and the radius $r$, constrained from the shortest observed variability timescale for this time period (see Section 3.1). The other six parameters define the EED and are the electron density $k_e$, the initial and final spectral indices $p1$ and $p2$, the break Lorentz factor of the electron distribution $\gamma_b$, and the minimum and maximum Lorentz factors of the EED $\gamma_{min}$ and $\gamma_{max}$. More details of the parameters can be found in Nigro et al. (2022).

The parameters $\delta$, $r$, $\gamma_{min}$, and $\gamma_{max}$ are kept fixed, while the other parameters are left free during the fitting procedure. To limit the span of the parameter space, we fit the $\log_{10}$ of the parameters whose range is expected to cover several orders of magnitude, namely $k_e$, $\gamma_b$, and $B$. The fit is performed using the Markov Chain Monte Carlo (MCMC) method (Gamerman & Lopes 2006; Hogg & Foreman-Mackey 2018). The MCMC sampling was run for 5000 steps with 30 walkers (six times the number of free parameters), with the first 2000 steps discarded as a burn-in period. The values of the parameters are reported in Table 2. As seen in Figure 6, a simple one-zone synchrotron and SSC radiation model describes the data well, with a good

agreement seen between the fitted model and the data over the energy range considered.

## 4. Conclusions

In this work, we report the follow-up to the discovery of VHE emission from S3 1227+25 with VERITAS and undertake a temporal and spectral analysis of the multiwavelength data during this period, in particular the gamma-ray observations. The shortest observed variability timescale obtained with the Fermi-LAT for S3 1227+25 during the VERITAS detection is $\tau_{obs} = 6.2 \pm 0.9$ hr. A joint fit to the combined gamma-ray spectrum was found not to favor a PL, LP, or PL with an exponential cutoff model significantly.

The cross-correlation studies between the gamma-ray and radio light curves show a positive correlation, significant at a level of above $3\sigma$, and consistent with zero time lag. Moreover, a positive correlation, significant at a level of above $3\sigma$ and consistent with zero time lag, is also seen between Fermi-LAT data and ATLAS and ASAS-SN $g$ data, while we find evidence of a broader peaked correlation, also compatible with a zero lag, between Fermi-LAT and ASAS-SN $V$ observations. The final method that sheds light on the mechanisms responsible for the VERITAS detection of S3 1227+25 was modeling the multiwavelength SED taken between 2015 May 16 and 18. We consider a simple one-zone synchrotron and SSC radiation model consisting of a single blob accelerating with a broken PL EED. A good agreement was seen between the fitted model and the multiwavelength spectral data over the entire energy range considered.

The results of all the investigations, put together, lead to the natural conclusion that a one-zone SSC model explains the gamma-ray observations of S3 1227+25 during the VERITAS detection. There is evidence to suggest a compact emission region, namely the short variability timescales. Furthermore, the cross-correlation studies between the different light curves, in particular the strong optical and gamma-ray correlations, also suggest a single-zone model of emission. This result is further reinforced by evidence that the multiwavelength SED is well described by a simple one-zone leptonic SSC radiation model.

### ORCID iDs

A. Acharyya https://orcid.org/0000-0002-2028-9230
C. B. Adams https://orcid.org/0000-0002-9021-6192
P. Bangale https://orcid.org/0000-0002-3886-3739
W. Benbow https://orcid.org/0000-0003-2098-170X
A. Brill https://orcid.org/0000-0002-6208-5244
M. Errando https://orcid.org/0000-0002-1853-863X
A. Falcone https://orcid.org/0000-0002-5068-7344
Q. Feng https://orcid.org/0000-0001-6674-4238
G. M. Foote https://orcid.org/0000-0002-2944-6060
L. Fortson https://orcid.org/0000-0002-1067-8558
A. Furniss https://orcid.org/0000-0003-1614-1273
W. Hanlon https://orcid.org/0000-0002-0109-4737
D. Hanna https://orcid.org/0000-0002-8513-5603
O. Hervet https://orcid.org/0000-0003-3878-1677
C. E. Hinrichs https://orcid.org/0000-0001-6951-2299
J. Holder https://orcid.org/0000-0002-6833-0474
W. Jin https://orcid.org/0000-0002-1089-1754
M. N. Johnson https://orcid.org/0009-0008-2688-0815
P. Kaaret https://orcid.org/0000-0002-3638-0637
D. Kieda https://orcid.org/0000-0003-4785-0101
T. K. Kleiner https://orcid.org/0000-0002-4260-9186
N. Korzoun https://orcid.org/0000-0002-4289-7106
M. J. Lang https://orcid.org/0000-0003-4641-4201
M. Lundy https://orcid.org/0000-0003-3802-1619
G. Maier https://orcid.org/0000-0001-9868-4700
M. J. Millard https://orcid.org/0000-0001-7106-8502
C. L. Mooney https://orcid.org/0000-0001-5937-446X

P. Moriarty https://orcid.org/0000-0002-1499-2667
R. Mukherjee https://orcid.org/0000-0002-3223-0754
S. O'Brien https://orcid.org/0000-0002-9296-2981
R. A. Ong https://orcid.org/0000-0002-4837-5253
M. Pohl https://orcid.org/0000-0001-7861-1707
E. Pueschel https://orcid.org/0000-0002-0529-1973
J. Quinn https://orcid.org/0000-0002-4855-2694
K. Ragan https://orcid.org/0000-0002-5351-3323
D. Ribeiro https://orcid.org/0000-0002-7523-7366
I. Sadeh https://orcid.org/0000-0003-1387-8915
A. C. Sadun https://orcid.org/0000-0001-8086-7242
L. Saha https://orcid.org/0000-0002-3171-5039
M. Santander https://orcid.org/0000-0001-7297-8217
R. Shang https://orcid.org/0000-0002-9856-989X
M. Splettstoesser https://orcid.org/0000-0003-3407-9936
D. A. Williams https://orcid.org/0000-0003-2740-9714
S. L. Wong https://orcid.org/0000-0002-2730-2733
Talvikki Hovatta https://orcid.org/0000-0002-2024-8199
Svetlana G. Jorstad https://orcid.org/0000-0001-6158-1708
Sebastian Kiehlmann https://orcid.org/0000-0001-6314-9177
Anne Lähteenmäki https://orcid.org/0000-0002-0393-0647
Ioannis Liodakis https://orcid.org/0000-0001-9200-4006
Alan P. Marscher https://orcid.org/0000-0001-7396-3332
Walter Max-Moerbeck https://orcid.org/0000-0002-5491-5244
Anthony C. S. Readhead https://orcid.org/0000-0001-9152-961X
Rodrigo Reeves https://orcid.org/0000-0001-5704-271X
Paul S. Smith https://orcid.org/0000-0002-5083-3663
Merja Tornikoski https://orcid.org/0000-0003-1249-6026

## References

Abdo, A. A., Ackermann, M., Agudo, I., et al. 2010, ApJ, 716, 30
Abdollahi, S., Acero, F., Baldini, L., et al. 2022, ApJS, 260, 53
Abeysekara, A. U., Benbow, W., Bird, R., et al. 2020, ApJ, 890, 97
Acharyya, A., Chadwick, P. M., & Brown, A. M. 2021, MNRAS, 500, 5297
Ackermann, M., Ajello, M., Allafort, A., et al. 2013, ApJS, 209, 34
Ackermann, M., Ajello, M., Atwood, W. B., et al. 2015, ApJ, 810, 14
Ackermann, M., Ajello, M., Atwood, W. B., et al. 2016a, ApJS, 222, 5
Ackermann, M., Anantua, R., Asano, K., et al. 2016b, ApJL, 824, L20
Aharonian, F., Akhperjanian, A. G., Anton, G., et al. 2009, A&A, 502, 749
Aharonian, F. A. 2002, MNRAS, 332, 215
Ajello, M., Atwood, W. B., Baldini, L., et al. 2017, ApJS, 232, 18
Akaike, H. 1974, ITAC, 19, 716
Albert, J., Aliu, E., Anderhub, H., et al. 2007, ApJ, 669, 862
Atwood, W., Albert, A., Baldini, L., et al. 2013, arXiv:1303.3514
Atwood, W. B., Abdo, A. A., Ackermann, M., et al. 2009, ApJ, 697, 1071
Bade, N., Fink, H. H., & Engels, D. 1994, A&A, 286, 381
Beasley, A. J., Gordon, D., Peck, A. B., et al. 2002, ApJS, 141, 13
Becerra, J. 2015, ATel, 7596, 1
Berge, D., Funk, S., & Hinton, J. 2007, A&A, 466, 1219
Bromberg, O., & Levinson, A. 2009, ApJ, 699, 1274
Burnham, K., & Anderson, D. 2001, Wildlife Res., 28, 111
Burrows, D. N., Hill, J. E., Nousek, J. A., et al. 2005, SSRv, 120, 165
Cogan, P. 2008, ICRC (Mérida), 30, 1385
Cutini, S., & Gasparrini, D. 2015, ATel, 6982, 1
Dermer, C. D., & Giebels, B. 2016, CRPhy, 17, 594
Dermer, C. D., & Menon, G. 2009, High Energy Radiation from Black Holes: Gamma Rays, Cosmic Rays, and Neutrinos (Princeton, NJ: Princeton Univ. Press)
Dermer, C. D., Yan, D., Zhang, L., Finke, J. D., & Lott, B. 2015, ApJ, 809, 174
Dixon, R. S., & Kraus, J. D. 1968, AJ, 73, 381
Domínguez, A., Primack, J. R., Rosario, D. J., et al. 2011, MNRAS, 410, 2556
Donea, A. C., & Protheroe, R. J. 2003, PThPS, 151, 186
Edelson, R. A., & Krolik, J. H. 1988, ApJ, 333, 646
Emmanoulopoulos, D., McHardy, I. M., & Papadakis, I. E. 2013, MNRAS, 433, 907
Fan, J. H., Yang, J. H., Liu, Y., et al. 2016, ApJS, 226, 20
Finke, J. D., Dermer, C. D., & Böttcher, M. 2008, ApJ, 686, 181
Fomin, V., Fennell, S., Lamb, R., et al. 1994, APh, 2, 151
Foschini, L., Ghisellini, G., Tavecchio, F., Bonnoli, G., & Stamerra, A. 2011, A&A, 530, A77
Gaidos, J. A., Akerlof, C. W., Biller, S., et al. 1996, Natur, 383, 319
Gamerman, D., & Lopes, H. 2006, Markov Chain Monte Carlo: Stochastic Simulation for Bayesian Inference (2nd ed.; Boca Raton, FL: CRC Press)
Gehrels, N. 2004, in AIP Conf. Ser. 727, Gamma-Ray Bursts: 30 Years of Discovery, ed. E. Fenimore & M. Galassi (Melville, NY: AIP), 637
Giannios, D. 2013, MNRAS, 431, 355
Giannios, D., Uzdensky, D. A., & Begelman, M. C. 2009, MNRAS, 395, L29
Goldoni, P. 2021, Zenodo, doi:10.5281/zenodo.4721386
Harris, J., Daniel, M. K., & Chadwick, P. M. 2012, ApJ, 761, 2
Hogg, D. W., & Foreman-Mackey, D. 2018, ApJS, 236, 11
Holder, J. 2011, ICRC, 11, 137
Jones, T. W., O'Dell, S. L., & Stein, W. A. 1974, ApJ, 188, 353
Jorstad, S. G., Marscher, A. P., Larionov, V. M., et al. 2010, ApJ, 715, 362
Kharb, P., Gabuzda, D., & Shastri, P. 2008, MNRAS, 384, 230
Kochanek, C. S., Shappee, B. J., Stanek, K. Z., et al. 2017, PASP, 129, 104502
Krause, M., Pueschel, E., & Maier, G. 2017, APh, 89, 1
Krawczynski, H., Hughes, S. B., Horan, D., et al. 2004, ApJ, 601, 151
Lewis, F., Butler, A., & Gilbert, L. 2011, Meth. Ecol. Evol., 2, 155
Li, T.-P., & Ma, Y.-Q. 1983, ApJ, 272, 317
Lister, M. L., Homan, D. C., Kellermann, K. I., et al. 2021, ApJ, 923, 30
Liu, H. T., & Bai, J. M. 2006, ApJ, 653, 1089
Maier, G., & Holder, J. 2017, 35th ICRC, 301, 747
Mannheim, K., & Biermann, P. L. 1992, A&A, 253, L21
Maraschi, L., Ghisellini, G., & Celotti, A. 1992, ApJL, 397, L5
Marscher, A. P., & Jorstad, S. G. 2021, Galax, 9, 27
Massaro, F., Landoni, M., D'Abrusco, R., et al. 2015, A&A, 575, A124
Max-Moerbeck, W., Richards, J. L., Hovatta, T., et al. 2014, MNRAS, 445, 437
Meyer, M., Scargle, J. D., & Blandford, R. D. 2019, ApJ, 877, 39
Mukherjee, R. 2015, ATel, 7516, 1
Nalewajko, K. 2013, MNRAS, 430, 1324
Nass, P., Bade, N., Kollgaard, R. I., et al. 1996, A&A, 309, 419
Nieppola, E., Tornikoski, M., & Valtaoja, E. 2006, A&A, 445, 441
Nigro, C., Sitarek, J., Gliwny, P., et al. 2022, A&A, 660, A18
Padovani, P., & Giommi, P. 1995, MNRAS, 277, 1477
Paiano, S., Landoni, M., Falomo, R., et al. 2017, ApJ, 837, 144
Park, N. & VERITAS Collaboration 2015, 34th ICRC, 34, 771
Pauliny-Toth, I. I. K., & Kellermann, K. I. 1972, AJ, 77, 797
Poutanen, J., & Stern, B. 2010, ApJL, 717, L118
Resconi, E., Franco, D., Gross, A., Costamante, L., & Flaccomio, E. 2009, A&A, 502, 499
Richards, J. L., Max-Moerbeck, W., Pavlidou, V., et al. 2011, ApJS, 194, 29
Roming, P. W. A., Kennedy, T. E., Mason, K. O., et al. 2005, SSRv, 120, 95
Roming, P. W. A., Koch, T. S., Oates, S. R., et al. 2009, ApJ, 690, 163
Saito, S., Tanaka, Ł., Stawarz, Y. T, et al. 2013, ApJL, 766, L11
Schlafly, E. F., & Finkbeiner, D. P. 2011, ApJ, 737, 103
Shappee, B. J., Prieto, J. L., Grupe, D., et al. 2014, ApJ, 788, 48
Shaw, M. S., Romani, R. W., Cotter, G., et al. 2013, ApJ, 764, 135
Sikora, M., Begelman, M. C., & Rees, M. J. 1994, ApJ, 421, 153
Smith, P. S., Montiel, E., Rightley, S., et al. 2009, arXiv:0912.3621
Sokolov, A., Marscher, A. P., & McHardy, I. M. 2004, ApJ, 613, 725
Stern, B. E., & Poutanen, J. 2014, ApJ, 794, 8
Teraesranta, H., Tornikoski, M., Mujunen, A., et al. 1998, A&AS, 132, 305
Tonry, J. L., Denneau, L., Heinze, A. N., et al. 2018, PASP, 130, 064505
Welsh, W. F. 1999, PASP, 111, 1347
Wood, M., Caputo, R., Charles, E., et al. 2017, 35th ICRC (Busan), 35, 824
Wu, Z.-Z., Gu, M.-F., & Jiang, D.-R. 2009, RAA, 9, 168
Zhou, R. X., Zheng, Y. G., Zhu, K. R., & Kang, S. J. 2021, ApJ, 915, 59